Mitigating positional dependence in coplanar electrode Coulter-type microfluidic devices

Vito Errico [a,1], Adele De Ninno [a,1], Francesca Romana Bertani [b], Luca Businaro [b], Paolo Bisegna [a,*], Federica Caselli [a,*]

[a] *Department of Civil Engineering and Computer Science, University of Rome Tor Vergata, 00133 Rome, Italy*
[b] *Institute for Photonics and Nanotechnologies, Italian National Research Council, 00156 Rome, Italy*

ARTICLE INFO

ABSTRACT

Microfluidic impedance-based devices with coplanar electrode layout represent an attractive tool for low-cost, label-free, single-cell analysis. However, their usefulness has long been limited by the positional dependence of the measured signals, i.e., identical particles traveling along different paths provide different traces. In this paper we show that it is possible to significantly reduce this unwanted effect via straightforward signal processing, by exploiting the richness of the information contained in the recorded traces.

© 2017 The Author(s). Published by Elsevier B.V. This is an open access article under the CC BY-NC-ND license (http://creativecommons.org/licenses/by-nc-nd/4.0/).

1. Introduction

Coulter cytometers count and size particles by measuring the variations in electrical impedance that the particles cause when displacing a conductive fluid in an electric field [1]. Displaced volume is measured as a voltage pulse, whose magnitude provides information on the size of the particle.

During the last few years, there has been a growing interest in developing micro-scaled particle detectors based on the Coulter principle, due to their potential application to cell detection and analysis, which may be implemented as label-free alternative to flow cytometry instruments [2]. The transition to microfluidic systems facilitated the development of microchip impedance spectroscopy, a method that allows cell counting and sizing combined with the ability to differentiate between cell types by multi-frequency impedance measurements (e.g., [3–10]). In particular, at low frequencies the technique provides cell sizing because the impedance signal is proportional to cell volume. Higher frequency impedance measurements (1–5 MHz in saline) give information on the cell membrane capacitance, whilst frequencies above several MHz probe the internal properties of the cell [11].

Microfabricated impedance chips typically consist of microfluidic channels with integrated microelectrodes in coplanar or parallel-facing configurations [12]. Parallel-facing configurations have electrodes on both the top and the bottom of the channel, thus requiring the patterning of two separate substrates and their aligned bonding [13], which requires advanced equipment. On the other hand, coplanar electrodes are attractive since they can be easily patterned at very small dimensions yielding miniaturized, reproducible, and ultimately low-cost devices [14,15].

The resolution of Coulter-type devices is limited by the variability in the particle path through the sensing region [12,16,17]. In fact, due to a non-homogeneous electric field distribution, nominally identical particles flowing through different trajectories experience different electric field strengths and generate different impedance signals [11].

In order to mitigate the resulting error in the estimated particle size, great effort has been devoted towards the development of particle focusing approaches, with the purpose of aligning particles through the same trajectory (e.g., sheath flow [18], inertial focusing [19–21], dielectrophoresis [22–24], acoustophoresis [8], and hybrid approaches [25,26]). We have recently introduced a focusing-free approach for the parallel electrode configuration [27]. That method uses multiple pairs of facing electrodes to measure the transit time of particles through the sensing region using two simultaneous current measurements having different spatial orientation (i.e., transverse to channel axis and oblique). By comparing the transit times relevant to transverse and oblique signals, an

estimate of the vertical position of the particle is obtained, that is used to effectively compensate for the non-uniform electric field in the channel. However, that approach cannot be directly transferred to a coplanar layout, which on the other hand is even more sensitive to measurement inaccuracy due to positional dependence [28,29].

In this paper, we propose a method that significantly increases the size-estimation accuracy of standard coplanar electrode configurations without the need for particle focusing. It exploits the richness of the information contained in the measured signal traces, and hinges on a straightforward compensation strategy.

2. Materials and methods

2.1. Working principle

The schematic representation of a typical microfluidic impedance chip with coplanar electrodes is pictured in Fig. 1(a). The microchannel is filled with a conductive fluid, an AC voltage signal is applied at the central electrode, and the difference in current collected from the lateral electrodes is measured. The passage of a flowing particle is recorded as a pair of opposite peaks [31]. In fact, the differential current is maximal [resp. minimal] when the particle is approximately half-way between the left [resp. right] electrode and the central electrode, where the electric field strength is higher (Fig. 1(b)). Peak amplitude is a measure of
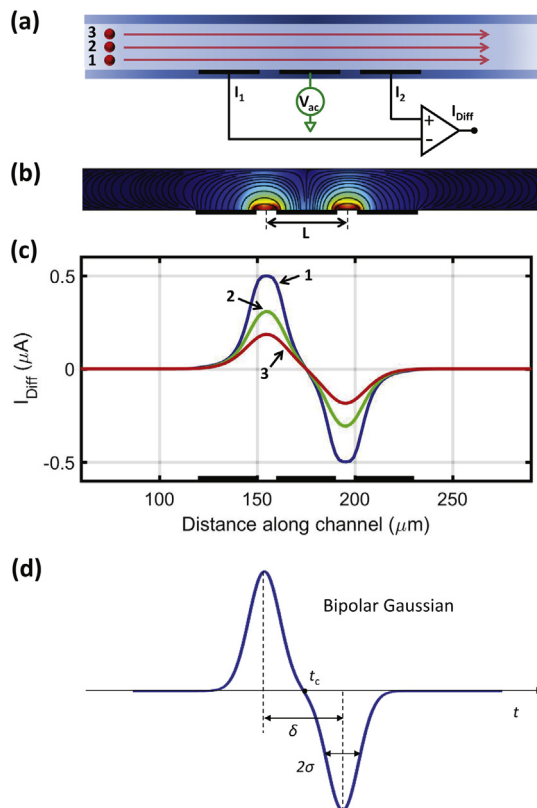
Fig. 1. Typical coplanar electrode microfluidic impedance chip. (a) Schematic representation (side view): AC excitation signals are applied to the central electrode, and the difference in current flowing through the lateral electrodes is measured, $I_{Diff} = I_2 - I_1$. (b) Typical current lines and electric field magnitude distribution. (c) Differential signals (real part) generated by a particle passing through the sensing region of the device at three different heights: close to the electrodes (curve 1), through the middle of the channel (curve 2), and close to the top of the channel (curve 3). Finite element simulation results (details of model equations can be found e.g. in [30]). (d) Bipolar Gaussian template used as event fitting function.

particle volume [11]. However, the electric field strength decreases away from the electrodes, and therefore identical particles traveling close to the electrodes (curve 1), through the middle of the channel (curve 2), or close to the top of the channel (curve 3), respectively yield higher, intermediate, or lower peak amplitudes (Fig. 1(c)).

A bipolar Gaussian profile [31,32] can be used to fit the differential signal traces (Fig. 1(d)):

$$s(t) = a[e^{g_+(t)} - e^{g_-(t)}], \qquad (1)$$

with

$$g_\pm(t) = \frac{-(t - (t_c \pm (\delta/2)))^2}{2\sigma^2}. \qquad (2)$$

This template depends on four parameters: central time moment, t_c; transit time, δ; peak width control, σ; and peak amplitude control, a.

The cube root of a can be used to estimate particle diameter:

$$D = Ga^{1/3}, \qquad (3)$$

where G is a gain factor to account for the electronic circuitry ($G = 10.5\,\mu m/\mu A^{1/3}$ for the present experimental setup). Accordingly, D is referred to in the following as "electrical" diameter. A significant spread in D is found even for a monodisperse particle population, due to the positional dependence issue. The transit time δ can be used to estimate particle velocity v [3]:

$$v = \frac{L}{\delta}, \qquad (4)$$

where L is the electrode pitch (Fig. 1(b)). Particle velocity v reflects particle position through the channel (i.e., a particle near the walls moves more slowly than one travelling in the centre). However, the velocity profile in the channel cross section is quite different from the signal amplitude distribution of identical particles flowing at different positions (ESI, Figure S1). As a consequence, particle velocity v alone cannot be used to compensate for the spread in signal amplitude [27].

On the other hand, by analyzing the pulse curve shapes (Fig. 1(c)), it is possible to determine approximately where in the channel a particle was travelling [33,8]. In particular, particles traveling close to the electrodes yield narrower pulses than particles traveling far from the electrodes. This suggests that the shape parameter σ/δ, i.e. the peak width control σ normalized by the particle transit time δ, is a metric correlating with particle trajectory (see also ESI, Figure S2). This shape parameter has been used in [33] to discard particles travelling in the lower half of a microfluidic channel with parallel-facing electrodes, reducing the coefficient of variation (CV) of any single population, at the expense of halving the throughput. In Section 3 we demonstrate for the first time how the metric σ/δ can be used to implement a straightforward compensation procedure, able to effectively mitigate the positional dependence of the measured traces.

2.2. Chip design and fabrication

The microfluidic chip was fabricated using standard microfabrication techniques. It is made of a polydimethylsiloxane (PDMS) block containing the microfluidic channel, bonded to a glass slide with deposited Ti/Au microelectrodes (20 nm / 200 nm). The PDMS microchannels were replica molded from photolithographically patterned SU-8 molds, while the electrodes were deposited on glass using optical lithography, e-beam evaporation and lift off procedures. In the sensing region the channel is 40 μm wide and 21 μm high; electrodes width in the flow direction is 30 μm, with a 10 μm
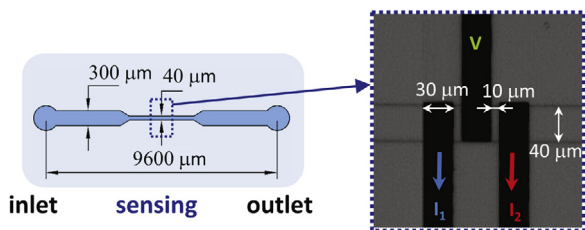
Fig. 2. Fluidic layout (top view) and bright field image of the gold electrodes in the sensing region (channel width, 40 μm; channel height, 21 μm).

spacing (Fig. 2). A custom chip holder is used for fluidic and electric connections.

2.3. Sample preparation

The proposed approach is described and validated by means of polystyrene beads (Sigma-Aldrich and PolySciences). In particular, beads with diameters of 5.2, 6, and 7 μm were suspended in PBS (phosphate-buffered saline) with 0.1% Tween 20 to avoid bead aggregation, and sufficient sucrose to match the density of the beads (1.05 g/cm^3). Sample conductivity was 1.1 S/m. The beads were sonicated prior to experiments in order to reduce cluster formation.

Moreover, as a proof-of-concept application, we considered Baker's yeast (*Saccharomyces cerevisiae*), which is one of the most intensively studied eukaryotic model organisms in molecular and cell biology [34]. Fresh yeasts were bought in a local grocery and suspended in a PBS buffer containing 0.1% BSA (bovine serum albumin) to avoid sticking to the channel wall, and enough sucrose to achieve neutral buoyancy. Sample conductivity was 0.8 S/m. A standard Trypan Blue assay was performed to confirm yeasts viability. Visual inspections in a cell counting chamber revealed a negligible number of budding cells. For internal reference, the sample was spiked with 6 μm diameter beads (distinguishable from the yeasts by means of opacity [35]).

2.4. Experimental setup

The sample was pumped into the microfluidic chip by a syringe pump (Harvard Apparatus) operating at 10 μl/min. An inline biocompatible filter with 10 μm porosity was used to prevent the risk of channel clogging. An impedance spectroscope (HF2IS,[2] Zurich Instruments) was used to apply an AC voltage signal (4 V amplitude) to the central electrode, and to demodulate the differential signal collected from the lateral electrodes and conditioned by a transimpedance amplifier (HF2TA, Zurich Instruments). A stimulation frequency of 1 MHz was used for the bead suspension [27], whereas yeast measurements were performed at 0.5 MHz [36,24,37]. A PC was used for instrument control and signal processing. Event detection in the datastream and segmentation were performed with the algorithm described in [32], and a Matlab script was used for fitting the template reported in Eq. (1) to event traces.

3. Results and discussion

3.1. Experiments with polystyrene beads

Bead populations with diameters of 5.2, 6 and 7 μm, respectively, were separately passed into the device at a concentration of

approximately 10^6 beads/ml. For each event detected by the segmentation algorithm, the parameters a, σ, δ, needed to compute the electrical diameter D (Eq. (3)) and the shape parameter σ/δ, were obtained by fitting the bipolar Gaussian template (Eq. (1)) to the experimental trace. The histogram of the root mean squared error of the fit, normalized by peak amplitude control a, is reported in ESI, Figure S3.

Fig. 3(a)–(c) show the density plots of the shape parameter σ/δ against the electrical diameter D, respectively relevant to the 5.2, 6, and 7 μm diameter beads. For comparison purposes, those density plots are shown together in Fig. 3(d). It turns out that, for each bead population, the lower the shape parameter σ/δ, the higher the electrical diameter D.

For illustrative purposes, five exemplary events, labelled from A to E, were selected (Fig. 3(d)). In particular, the events A, C, D, respectively with high, intermediate, low values of the shape parameter σ/δ, were picked in the datastream generated by 6 μm diameter beads. Moreover, the events E, B, with the same electrical diameter than event C, were chosen in the datastreams generated by 5.2 and 7 μm diameter beads, respectively. The experimental traces of those events, as extracted from the relevant datastreams, are reported in Fig. 3(e)–(i) (blue line) along with their fitting template (red line). Events A, C, and D, though relevant to same size beads (6 μm), exhibit electrical diameters of 5.1 μm, 7.2 μm, and 8.3 μm, respectively. On the other hand, the shape parameters of their traces are 0.26, 0.23, and 0.20 respectively. These considerations suggest that bead A was traveling close to the top of the channel, bead C through the middle of the channel, and bead D close to the electrodes. Events B, C, and E, representing beads of different size (respectively, 7, 6, and 5.2 μm), have the same electrical diameter (7.2 μm). This is consistent with B traveling close to the top of the channel, C through the middle of the channel, and E close to the electrodes, as suggested by the different shape parameters of their traces (respectively, 0.26, 0.23, 0.20).

Fig. 4 collects the density plots of the shape parameter σ/δ against the electrical diameter D normalized by the nominal bead diameter d, for the three populations of beads. Because the measured signal is proportional to particle volume, those density plots overlap. A linear regression model is used to fit the data:

$$D/d = c_1 + c_2(\sigma/\delta), \qquad (5)$$

from where

$$d = \frac{D}{c_1 + c_2(\sigma/\delta)}. \qquad (6)$$

Data relevant to individual bead populations or all the populations together were considered, and the resulting fitting parameters c_1 and c_2 are reported in Table 1, along with the relevant coefficient of determination r^2. The latter turned out to be close to 1, showing that the variance in the normalized electrical diameter D/d is well predictable from the shape parameter σ/δ by using the linear regression model (5). Moreover, practically the same parameter values c_1 and c_2 were obtained from each population or the whole ensemble.

Fig. 5(a) and (b) show histograms of the electrical diameter of (a) individual particle populations and (b) a mixed sample comprising equal concentrations of each population. As expected, the distribution has a significant spread and skew due to the positional dependence issue [8], and it is hard to recognize the presence of three bead populations in the histogram of Fig. 5(b).

Eq. (6) was used to correct the raw data as follows:

$$D\text{-corr} = \frac{D}{c_1 + c_2(\sigma/\delta)}, \qquad (7)$$

where c_1 and c_2 are reported in Table 1 (last row). The efficacy and effectiveness of this simple compensation method is evident from
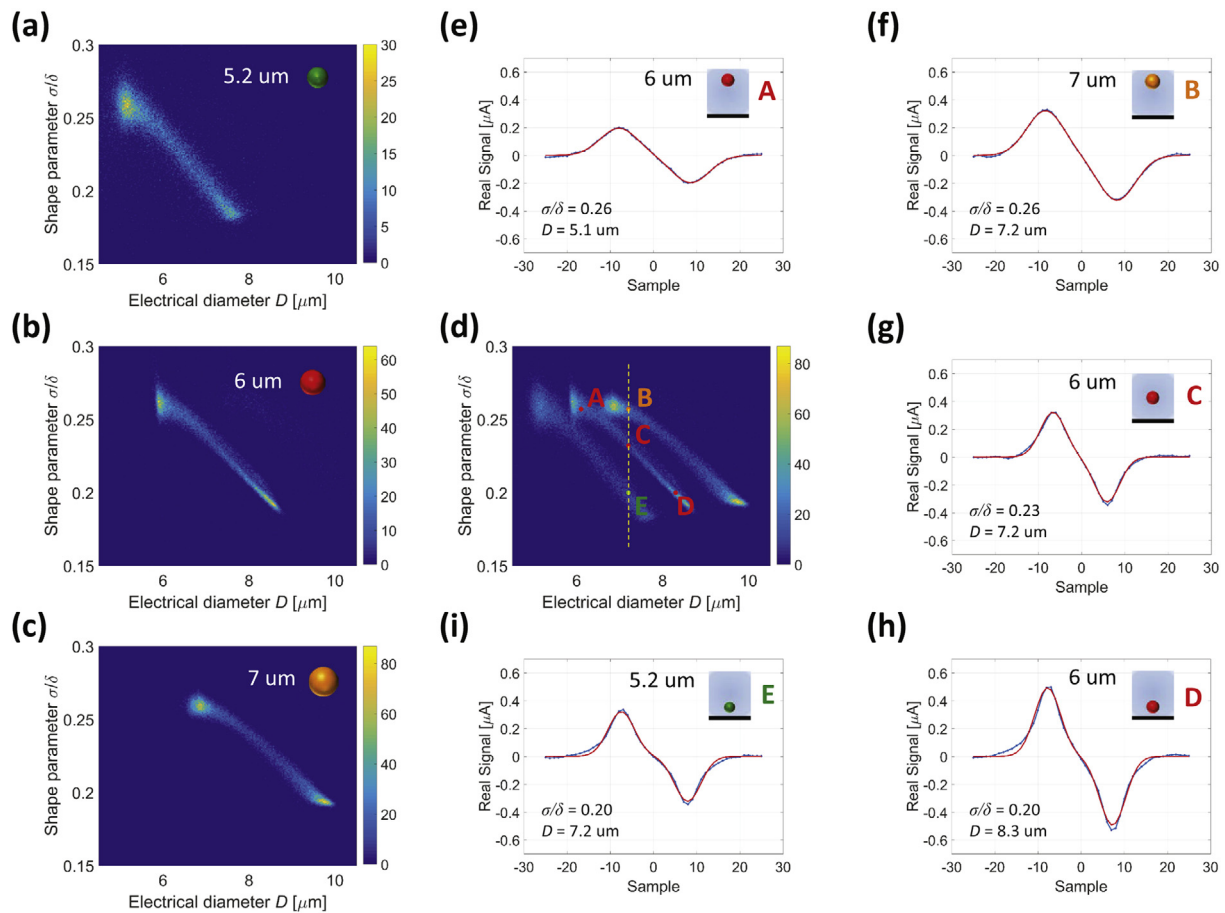
Fig. 3. Density plot of populations of beads with different sizes, with the shape parameter σ/δ plotted against the electrical diameter D. (a) 5.2 μm diameter beads, (b) 6 μm diameter beads, (c) 7 μm diameter beads. The density plots are shown together in (d), where exemplary events are labelled from A to E. The relevant traces (real part) are respectively shown in (e)–(i) (experimental trace, blue line; fitting template, red line), along with a side view cartoon. (For interpretation of the references to color in this figure legend, the reader is referred to the web version of this article.)
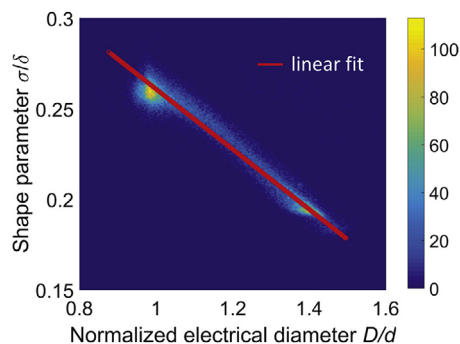
Fig. 4. Density plot of the shape parameter σ/δ against the electrical diameter D normalized by the nominal bead diameter d. The density plots relevant to the three populations of beads separately measured are plotted together and overlap. The linear fit $D/d = c_1 + c_2(\sigma/\delta)$ is shown as red line (fit parameters reported in Table 1, last row). (For interpretation of the references to color in this figure legend, the reader is referred to the web version of this article.)

the histograms of Fig. 5(d) and (e), where the three bead populations of different size are clearly identifiable. Fitting a Gaussian allows the CVs to be calculated as follows: 4.1%, 1.8%, and 1.9%, for the 5.2, 6, and 7 μm diameter beads respectively.[3] It is emphasized

___

[3] Manufacturers' quoted values are 2.6%, 10.0%, and 1.7%, respectively. The 10.0% CV of the 6 μm diameter beads from PolySciences is probably a conservative estimate.

that these values were obtained without using any particle focusing system. Similar values were reported by other groups that use impedance in combination with external force fields to position particles. Reported CV's include 1.8% (dielectric focusing of 6 μm particles, manufacturer's CV 1.2%) [13], and 2.04% [resp. 1.50%] (acoustic focusing of 7 μm particles, after removing 3.8% [resp. 5%] extremal events, manufacturer's CV <2.0%) [8].

Fig. 5(c) and (f) show density plots of particle velocity versus electrical diameter for the mixture of beads (raw data in (c) and corrected data in (f)), demonstrating that this simple algorithm significantly reduces the height dependent variation in impedance, i.e. all particles of a given size range have similar corrected electrical diameter irrespective of their trajectory through the channel.

In order to assess the performance of the proposed method over a broader particle size range, experimental measurements relevant to a mixture of 3, 6 and 10.1 μm diameter beads have been carried out, using 4, 2, or 1 V stimulation amplitude (see ESI, Figure S4).

Table 1
Parameters of the linear regression model $D/d = c_1 + c_2(\sigma/\delta)$ used to fit data plotted in Fig. 4 (individual bead populations or whole ensemble), and coefficient of determination r^2 of the regression.

| d [μm]	c_1	c_2	r^2
5.2	2.57	−6.01	0.93
6.0	2.61	−6.09	0.96
7.0	2.57	−6.07	0.97
All	2.57	−6.03	0.95
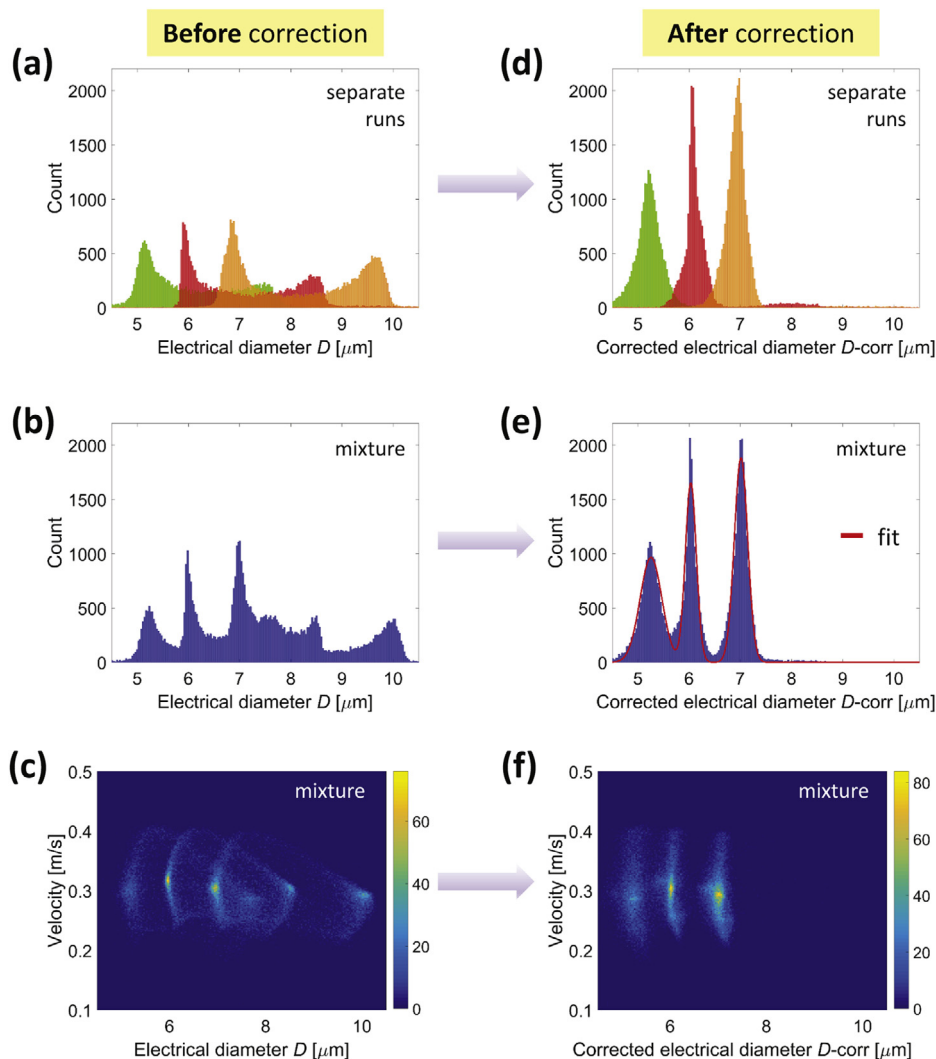
Fig. 5. Histogram of the electrical diameter of 5.2, 6 and 7 μm diameter beads measured (a) separately and (b) together. The data corrected according to Eq. (7) is presented in (d) and (e). Density plots of particle velocity vs electrical diameter for the mixture of beads (c) before and (f) after correction.

The values of the parameters c_1 and c_2 used to compute the corrected electrical diameter D-corr (Eq. (7)) generally depend on the experimental setup (e.g., buffer conductivity, stimulation frequency, electrode impedance). For a given setup, they can be obtained by means of a simple calibration procedure: (i) run the buffer spiked with a monodisperse bead population of nominal diameter d; (ii) obtain the relevant density plot of the shape parameter σ/δ against the normalized electrical diameter D/d (as in Fig. 4); (iii) fit the data to the linear model in Eq. (5).

3.2. Experiments with yeasts

The yeast preparation spiked with 6 μm diameter beads, described in Section 2.3, was then analyzed. Fig. 6 shows the density plot of the shape parameter σ/δ against the electrical diameter D. Besides the 6 μm diameter beads, two yeast populations can be recognized (see also ESI, Figure S5). Their presence, which is not evident in the histogram of the electrical diameter D reported in Fig. 7(a), becomes clear by applying the correction reported in Eq. (7). Indeed, Fig. 7(c) shows that the histogram of the corrected electrical diameter D-corr can be described as the superposition of
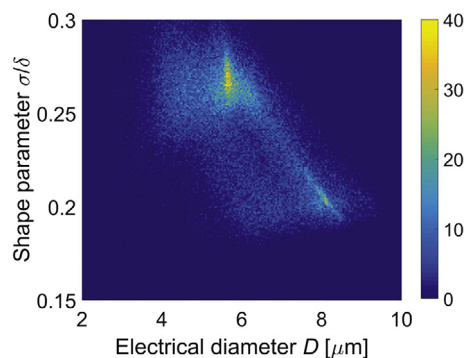
Fig. 6. _S. cerevisiae_ yeasts spiked with 6 μm diameter beads. Density plot of the shape parameter σ/δ against the electrical diameter D.

two Gaussian distributions with mean values of 4.6 ± 0.6 μm and 5.9 ± 0.5 μm. These findings are comparable with those reported in the literature [38]. Density plots of particle velocity versus electrical diameter are reported in Fig. 7(b) and (d), respectively for raw and corrected data.
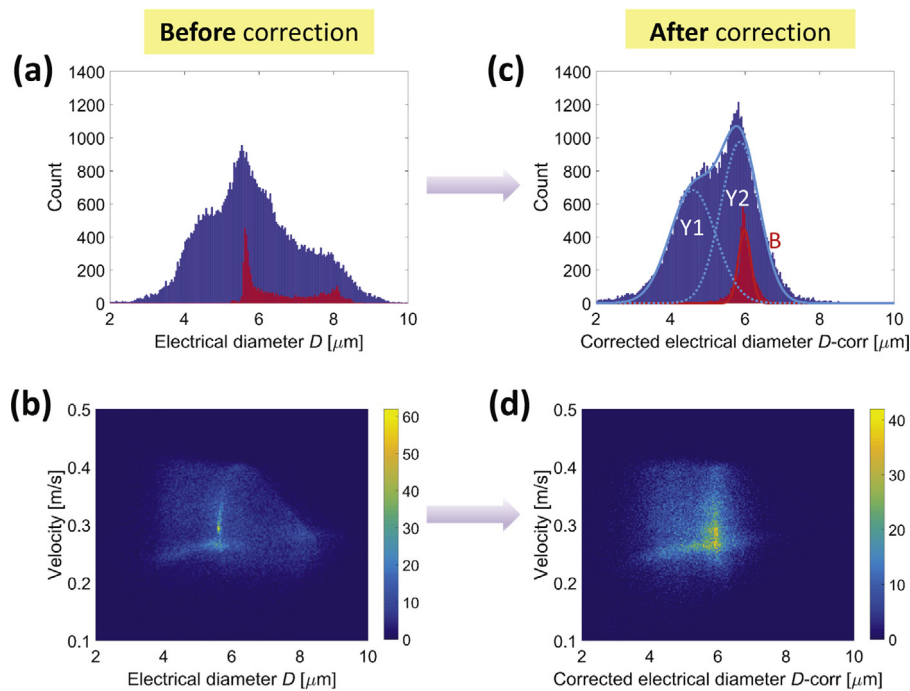
Fig. 7. *S. cerevisiae* yeasts spiked with 6 μm diameter beads. Histograms of the electrical diameter (a) before and (c) after correction (yeasts, blue bins; beads, red bins). In (c), fitting Gaussian distributions are also shown. Density plots of particle velocity vs electrical diameter (b) before and (d) after correction. (For interpretation of the references to color in this figure legend, the reader is referred to the web version of this article.)

4. Conclusions

In this work we have demonstrated a method that significantly reduces the positional dependence issue affecting Coulter-type microfluidic devices with coplanar layout. The proposed focusing-free approach requires trivial calibration of a given experimental setup together with straightforward signal-processing. The easiness of fabrication of coplanar electrodes coupled with the increased accuracy in particle sizing achieved by the proposed methodology make the resulting device a simple and effective tool for label-free particle analysis, with potential applications in medicine, life science and quality control.

Acknowledgements

Appendix A. Supplementary data

Supplementary data associated with this article can be found, in the online version, at http://dx.doi.org/10.1016/j.snb.2017.03.035.

References

[1] W. Coulter, Means for counting particles suspended in a fluid, US Patent 2,656,508 (1953).
[2] R. Rodriguez-Trujillo, M.A. Ajine, A. Orzan, M.D. Mar, F. Larsen, C.H. Clausen, W.E. Svendsen, Label-free protein detection using a microfluidic Coulter-counter device, Sens. Actuators B: Chem. 190 (2014) 922–927, http://dx.doi.org/10.1016/j.snb.2013.09.038.
[3] S. Gawad, L. Schild, P. Renaud, Micromachined impedance spectroscopy flow cytometer for cell analysis and particle sizing, Lab Chip 1 (1) (2001) 76–82, http://dx.doi.org/10.1039/B103933B.
[4] D. Holmes, T. Sun, J. Holloway, J. Cakebread, D. Davies, H. Morgan, Label-free differential leukocyte counts using a microfabricated, single-cell impedance spectrometer, in: Proceedings of the 6th Annual IEEE Sensor Conference, Hyatt Regency, Atlanta, USA, 2007, pp. 1452–1456.
[5] J.-L. Hong, K.-C. Lan, L.-S. Jang, Electrical characteristics analysis of various cancer cells using a microfluidic device based on single-cell impedance measurement, Sens. Actuators B: Chem. 173 (2012) 927–934, http://dx.doi.org/10.1016/j.snb.2012.06.046.
[6] G. Mernier, W. Hasenkamp, N. Piacentini, P. Renaud, Multiple-frequency impedance measurements in continuous flow for automated evaluation of yeast cell lysis, Sens. Actuators B: Chem. 170 (2012) 2–6, http://dx.doi.org/10.1016/j.snb.2010.10.050.
[7] S.-B. Huang, Y. Zhao, D. Chen, H.-C. Lee, Y. Luo, T.-K. Chiu, J. Wang, J. Chen, M.-H. Wu, A clogging-free microfluidic platform with an incorporated pneumatically driven membrane-based active valve enabling specific membrane capacitance and cytoplasm conductivity characterization of single cells, Sens. Actuators B: Chem. 190 (2014) 928–936, http://dx.doi.org/10.1016/j.snb.2013.09.070.
[8] C. Grenvall, C. Antfolk, C. Bisgaard, T. Laurell, Two-dimensional acoustic particle focusing enables sheathless chip Coulter counter with planar electrode configuration, Lab Chip 14 (24) (2014) 4629–4637, http://dx.doi.org/10.1039/C4LC00982G.
[9] S.C. Bürgel, C. Escobedo, N. Haandbæk, A. Hierlemann, On-chip electroporation and impedance spectroscopy of single-cells, Sens. Actuators B: Chem. 210 (2015) 82–90, http://dx.doi.org/10.1016/j.snb.2014.12.016.
[10] I. Heidmann, G. Schade-Kampmann, J. Lambalk, M. Ottiger, M. Di Berardino, Impedance flow cytometry: a novel technique in pollen analysis, PLOS ONE 11 (11) (2016) e0165531, http://dx.doi.org/10.1371/journal.pone.0165531.
[11] T. Sun, H. Morgan, Single-cell microfluidic impedance cytometry: a review, Microfluid. Nanofluid. 8 (4) (2010) 423–443, http://dx.doi.org/10.1007/s10404-010-0580-9.
[12] K.C. Cheung, M. Di Berardino, G. Schade-Kampmann, M. Hebeisen, A. Pierzchalski, J. Bocsi, A. Mittag, A. Tárnok, Microfluidic impedance-based flow cytometry, Cytometry Part A 77 (7) (2010) 648–666, http://dx.doi.org/10.1002/cyto.a.20910.
[13] G. Mernier, E. Duqi, P. Renaud, Characterization of a novel impedance cytometer design and its integration with lateral focusing by dielectrophoresis, Lab Chip 12 (21) (2012) 4344–4349, http://dx.doi.org/10.1039/c2lc40551b.
[14] J. Hong, D.S. Yoon, S.K. Kim, T.S. Kim, S. Kim, E.Y. Pak, K. No, AC frequency characteristics of coplanar impedance sensors as design parameters, Lab Chip 5 (3) (2005) 270–279, http://dx.doi.org/10.1039/B410325D.
[15] C.H. Clausen, G.E. Skands, C.V. Bertelsen, W.E. Svendsen, Coplanar electrode layout optimized for increased sensitivity for electrical impedance spectroscopy, Micromachines 6 (1) (2015) 110–120, http://dx.doi.org/10.3390/mi6010110.

[16] D. Spencer, H. Morgan, Positional dependence of particles in microfluidic impedance cytometry, Lab Chip 11 (7) (2011) 1234–1239, http://dx.doi.org/10.1039/c1lc20016j.

[17] M.A. Edwards, S.R. German, J.E. Dick, A.J. Bard, H.S. White, High-speed multipass Coulter counter with ultrahigh resolution, ACS Nano 9 (12) (2015) 12274–12282, http://dx.doi.org/10.1021/acsnano.5b05554.

[18] X. Mao, A. Nawaz, S. Lin, M. Lapsley, Y. Zhao, J. McCoy, W. El-Deiry, T. Huang, An integrated multiparametric flow cytometry chip using "microfluidic drifting" based three-dimensional hydrodynamic focusing, Biomicrofluidics 6 (2) (2012) 024113, http://dx.doi.org/10.1063/1.3701566.

[19] D. Di Carlo, Inertial microfluidics, Lab Chip 9 (21) (2009) 3038–3046, http://dx.doi.org/10.1039/b912547g.

[20] S. Hur, H. Tse, D. Di Carlo, Sheathless inertial cell ordering for extreme throughput flow cytometry, Lab Chip 10 (3) (2010) 274–280, http://dx.doi.org/10.1039/B919495A.

[21] R. Pugo, S. Deane, C. Glasse, M. Burcher, H. Morgan, C. Reccius, Flow speed particle focusing in microfluidic impedance measurements, in: A. Verpoorte, H. Andersson-Svahn, J. Emnéus (Eds.), 14th International Conference on Miniaturized Systems for Chemistry and Life Sciences, MicroTAS, 2010.

[22] D. Holmes, H. Morgan, N. Green, High throughput particle analysis: combining dielectrophoretic particle focussing with confocal optical detection, Biosens. Bioelectron. 21 (8) (2006) 1621–1630, http://dx.doi.org/10.1016/j.bios.2005.10.017.

[23] N. Haandbæk, O. With, S.C. Bürgel, F. Heer, A. Hierlemann, Resonance-enhanced microfluidic impedance cytometer for detection of single bacteria, Lab Chip 14 (17) (2014) 3313–3324, http://dx.doi.org/10.1039/C4LC00576G.

[24] M. Shaker, L. Colella, F. Caselli, P. Bisegna, P. Renaud, An impedance-based flow micro-cytometer for single cell morphology discrimination, Lab Chip 14 (14) (2014) 2548–2555, http://dx.doi.org/10.1039/c4lc00221k.

[25] M. Evander, B. Dura, A. Ricco, G. Kovacs, L. Giovangrandi, Signal improvement by dielectric focusing in microfluidic impedance cytometers, in: A. Verpoorte, H. Andersson-Svahn, J. Emnéus (Eds.), 14th International Conference on Miniaturized Systems for Chemistry and Life Sciences, MicroTAS, 2010.

[26] J. Zhang, S. Yan, G. Alici, N. Nguyen, D. Di Carlo, W. Li, Real-time control of inertial focusing in microfluidics using dielectrophoresis (DEP), RSC Adv. 4 (107) (2014) 62076–62085, http://dx.doi.org/10.1039/C4RA13075H.

[27] D. Spencer, F. Caselli, P. Bisegna, H. Morgan, High accuracy particle analysis using sheathless microfluidic impedance cytometry, Lab Chip 16 (13) (2016) 2467–2473, http://dx.doi.org/10.1039/c6lc00339g.

[28] T. Sun, N.G. Green, S. Gawad, H. Morgan, Analytical electric field and sensitivity analysis for two microfluidic impedance cytometer designs, IET Nanobiotechnol. 1 (5) (2007) 69–79, http://dx.doi.org/10.1049/iet-nbt:20070019.

[29] J. Riordon, N. M.-Catafard, M. Godin, Using the fringing electric field in microfluidic volume sensors to enhance sensitivity and accuracy, Appl. Phys. Lett. 101 (15) (2012) 154105, http://dx.doi.org/10.1063/1.4759033.

[30] F. Caselli, M. Shaker, L. Colella, P. Renaud, P. Bisegna, Modeling, simulation and performance evaluation of a novel microfluidic impedance cytometer for morphology-based cell discrimination, J. Microelectromech. Syst. 23 (4) (2014) 785–794, http://dx.doi.org/10.1109/JMEMS.2014.2325979.

[31] T. Sun, C. van Berkel, N.G. Green, H. Morgan, Digital signal processing methods for impedance microfluidic cytometry, Microfluid. Nanofluid. 6 (2) (2009) 179–187, http://dx.doi.org/10.1007/s10404-008-0315-3.

[32] F. Caselli, P. Bisegna, A simple and robust event-detection algorithm for single-cell impedance cytometry, IEEE Trans. Biomed. Eng. 63 (2) (2016) 415–422, http://dx.doi.org/10.1109/TBME.2015.2462292.

[33] D. Barat, D. Spencer, G. Benazzi, M.C. Mowlem, H. Morgan, Simultaneous high speed optical and impedance analysis of single particles with a microfluidic cytometer, Lab Chip 12 (1) (2012) 118–126, http://dx.doi.org/10.1039/C1LC20785G.

[34] S. Ostergaard, L. Olsson, J. Nielsen, Metabolic engineering of Saccharomyces cerevisiae, Microbiol. Mol. Biol. Rev. 64 (1) (2000) 34–50, http://dx.doi.org/10.1128/MMBR.64.1.34-50.2000.

[35] R.A. Hoffman, T.S. Johnson, W.B. Britt, Flow cytometric electronic direct current volume and radiofrequency impedance measurements of single cells and particles, Cytometry 1 (6) (1981) 377–384, http://dx.doi.org/10.1002/cyto.990010605.

[36] G. Schade-Kampmann, A. Huwiler, M. Hebeisen, T. Hessler, M. Di Berardino, On-chip non-invasive and label-free cell discrimination by impedance spectroscopy, Cell Prolifer. 41 (5) (2008) 830–840, http://dx.doi.org/10.1111/j.1365-2184.2008.00548.x.

[37] N. Haandbæk, S.C. Bürgel, F. Rudolf, F. Heer, A. Hierlemann, Characterization of single yeast cell phenotypes using microfluidic impedance cytometry and optical imaging, ACS Sens. 1 (8) (2016) 1020–1027, http://dx.doi.org/10.1021/acssensors.6b00286.

[38] F. Sherman, Getting started with yeast, in: C. Guthrie, G.R. Fink (Eds.), Guide to Yeast Genetics and Molecular Biology, Vol. 194 of Methods in Enzymology, Academic Press, 1991, pp. 3–21, http://dx.doi.org/10.1016/0076-6879(91)94004-V.

Biographies

Vito Errico is a Postdoctoral Researcher at the Department of Civil Engineering and Computer Science, University of Rome Tor Vergata. His research interests include design, fabrication and characterization of micro- and nano-systems.

Adele De Ninno is a Postdoctoral Researcher at the Department of Civil Engineering and Computer Science, University of Rome Tor Vergata. Her research interests include microfluidics-based approaches for mimicking complex biological processes, organs-on-chip and lab-on-chip devices for point-of-care diagnostic applications.

Francesca Romana Bertani is a Researcher at Institute for Photonics and Nanotechnologies, part of the Italian National Research Council. Her research interests involve the development of spectral imaging techniques and data analysis to perform label-free characterization of living cells and co-culture systems.

Luca Businaro is a micro and nanofabrication scientist at Institute for Photonics and Nanotechnologies, part of the Italian National Research Council. His primary scientific interest dwells in reconstituting on microfluidic chips complex biological systems such as the insult-immune system interface.

Paolo Bisegna is a Professor of Mechanics at the Department of Civil Engineering and Computer Science, and Director of the Medical Engineering Program, University of Rome Tor Vergata. His research interests include biomedical microdevices, biomechanics and computational mechanics.

Federica Caselli is a Researcher of Medical Engineering at the Department of Civil Engineering and Computer Science, University of Rome Tor Vergata. Her research interests include analysis and development of microdevices for biomedical use, computational biomechanics, and biomedical signal and image processing.